Journal of Marine Research, 57, 213–244, 1999

Journal of MARINE RESEARCH

Volume 57, Number 2

Mode waters and subduction rates in a high-resolution South Atlantic simulation

by Anne P. de Miranda[1], Bernard Barnier[1] and William K. Dewar[2]

ABSTRACT

Water mass production and destruction in the subtropical South Atlantic gyre is studied. A high resolution numerical model is used to examine regional mode water formation and estimate the associated instantaneous and mean subduction rates. Primitive equation dynamics expressed in depth following (sigma) coordinates are employed.

The main hydrographic and kinematic features of the South Atlantic are faithfully reproduced by the model. In particular, the principle current systems appear and the model exhibits a sequence of ventilated potential vorticity minima on density surfaces coinciding with those of observed South Atlantic mode waters. The formation sequence within the model of these mode waters is described. Net formation rates are estimated using a pseudo-Lagrangian method and by diagnosing the time history of subsurface water mass volumes.

Maximum formation rates occur in the density bands of the mode waters. It is argued that the roots of the model mode waters are found along open ocean late winter outcrops, rather than in the waters entering the gyre from the Brazil Current/Malvinas Current Confluence region. Eddies generate interannual variability in mode water formation and precondition the waters in the outcrop regions for convection. On the other hand, the eddy kinetic energy of the Confluence region is too intense to permit a direct connection between deep convection cells in the western boundary current and those in the open South Atlantic that directly form mode water.

1. Introduction

An interesting, and as yet poorly understood, aspect of the baroclinic structure of the ocean is its tendency to form and maintain mode waters. These are regions of minimum

1. Laboratoires des Écoulements Géophysiques et Industriels, Institut de Mécanique de Grenoble, BP 53 F-38041 Grenoble Cedex 09, France. ***email: anne.de-miranda@hmg.inpg.fr***

2. Department of Oceanography, Florida State University, Tallahahasse, Florida, 32306, U.S.A.

subsurface stratification within the ocean density field, representing anomalously large volumes of water with given density values. This latter characteristic has earned these waters the name "mode" waters, implying that such densities in some sense represent preferred density states for the open ocean. Observations supporting the existence of North Atlantic mode waters reach back well more than a century. More recently, McCartney (1977) suggested they are a generic feature of the world ocean. Unfortunately, the depth of our dynamical understanding of mode waters lags far behind our observational understanding. Only the most rudimentary theories of the combined buoyantly and mechanically driven circulation currently exist, and few numerical models have been analyzed from a mode-water perspective. The purpose of this paper is to contribute to the latter category; i.e., we report on the mode water performance of a large-scale numerical ocean model. The region being simulated is the South Atlantic, which given a plethora of mode waters is an ideal basin for such a study. The high spatial and temporal resolution of the model further allows for a careful examination of mode water dynamics and formation rates.

a. Background

The famous Challenger section, stretching from the Virgin Islands to Bermuda and finally to New York, is perhaps the first section to have identified mode waters. These appear as the anomalously thick layer of water found at a temperature of 18°C. Although clear in this section, the actual recognition of the phenomenon must be credited to Worthington, who in 1959 coined the term "18°C water" to describe it. Subsequently, a North Pacific pycnostad was described by Masuzawa (1969), and originated the term "mode water." Both of the above mode waters are found in subtropical gyres. McCartney (1977) described a brand of mode waters found in subpolar gyres, and later (McCartney, 1982) compared and contrasted the subpolar and subtropical mode water types. He suggested that subtropical mode waters were more confined in their distribution and also forwarded the idea that both types could be reliably traced in potential vorticity maps. He also argued that mode waters are a generic feature of the world ocean and found in all ocean basins.

Among the important observationally derived characteristics of mode waters is their remarkable stability in properties. Talley and Raymer (1982) and Jenkins (1982) show that North Atlantic mode water temperature and salinity have varied by 1.°C and 0.1 PSU over the last 45 years. The potential density surface characterizing North Atlantic mode waters in this same period varied by only 0.2 kg/m^3. The changes that did occur happened on the decadal time scale, in keeping with Warren (1972) who argued that mode water characteristics were insensitive to annual fluctuations in atmospheric forcing.

The dynamical explanation of mode waters remains somewhat less well developed. The potential vorticity basis for mode waters forwarded by McCartney is reminiscent of the ventilated thermocline theory (Luyten *et al.,* 1983) of the general circulation given the convective origins of the mode waters. A potential shortcoming of the ventilated thermocline as applied to mode waters is that eddies are ignored. In contrast, homogenization

theory (Rhines and Young, 1982) ignores diabatic inputs, but includes an explicit eddy parameterization. Dewar (1986) joined these two theories together in a generalized theory, which recognized mode waters as a natural consequence of anticyclonic circulation in the presence of buoyancy forcing. The decadal scale for property fluctuations of mode waters was accounted for in this theory, as was their distribution pattern. More recently, Samelson and Vallis (1997) in a numerical study of a planetary geostrophic model found a mode water-like stratification whose roots can be traced to the intergyre boundary.

A different approach to the quantitative description of water mass formation has been forwarded by Speer and Tziperman (1992). Using an approach first discussed by Walin (1982), they relate buoyancy fluxes at the sea surface to production rates. The connection is intrinsically pseudo-Lagrangian, especially in a time-dependent setting, because the net formation of a given density class is determined by the buoyancy fluxes acting within the mobile outcropping window. A premium is thus placed on accurate temporal and spatial buoyancy flux data in the Speer and Tziperman procedure. In spite of the many sources for error, the apparent skill of their approach is clear in that formation rate maxima for the North Atlantic occur in the density ranges of North Atlantic subtropical and subpolar mode water.

The Speer and Tziperman approach requires no flow field model. A technique for water mass production based on a ventilated thermocline model was proposed by Marshall *et al.* (1993) and Qiu and Huang (1995). Given wind stress data and density outcrop locations, they computed the rates of subducted water mass formation for the North Atlantic and North Pacific. A main point of their work was that seasonality induced preferred times for water mass formation in given density bands, an idea first suggested by Stommel (1979). Qiu and Huang (1995) also argued lateral induction, due to mixed layer base shallowing to the south, was an important effect in setting net formation rates.

b. South Atlantic mode waters

One of the earliest recognitions of mode waters in the southern hemisphere is due to McCartney (1977). Using Deacon's review (Deacon, 1937) and various hydrographic sections in the Southern Ocean, he described thick thermostads at 200 m depth just north of the Subantarctic Front all around the Antarctic. The characteristics of these thermostads vary traveling eastward: the temperature of the thick layer is around 14.5°C in the western South Atlantic and goes down to 4–5°C in the eastern South Pacific. These characteristics are similar to those of the winter deep mixed layer in the Subantarctic Zone (McCartney, 1982) and were named Subantarctic Mode Water (SAMW) (McCartney, 1977).

Once formed, SAMW is advected northwestward in the Southern Ocean by the prevailing subtropical gyres. The South Pacific subtropical gyre and South Indian gyre exhibit the presence of low potential vorticity layers of this type. In the South Atlantic, the signature of mode waters is weak, but was identified by McCartney (1977, 1982). A meridional section at 30W shows the presence of a thick 14°C thermostad located to the north of the Subantarctic Front (McCartney, 1977). A clear signature of SAMW has been

observed as far as 25W with temperature between 11.6 and 13.5°C, and salinity between 35.1 and 35.4 (densities from 26.72 to 26.6) (Tsuchiya *et al.,* 1994).

Subtropical Mode Waters (STMW) formed to the north of the Subtropical Front were found in the Confluence region (Provost *et al.,* 1995). These STMW were identified by their low potential vorticity signature at depth about 200–400 m. Their temperature was between 14.5 and 16°C, and their salinity between 35.5 and 36 ($\sigma_0 = 26.6$). Gordon (1981) suggests that the South Atlantic STMWs are formed by winter convection in the Brazil Current.

c. Ventilation: What is the role of mesoscale activity?

Mode waters form in very eddy-rich regions of the ocean. Indeed, the Confluence zone of the South Atlantic is perhaps the most mesoscale energetic region in the world ocean. While it is, therefore, likely that eddy activity plays a role in setting mode water properties and in mode water maintenance, exactly what this role is remains elusive. The (statistical) steady state theory in Dewar (1986) relates the persistence of mode water characteristics to eddy activity. This occurs principally by their role as diffusers of potential vorticity. Late winter convection and formation is viewed in this theory as a source of low potential vorticity. The subsequent diffusion of this signal into the subsurface subtropical gyre circulation sequesters the fluid in a "holding" pond, which then plays the role of the persistent mode water pool. As the pool integrates surface water properties in time, the pool properties are slow to change. Diffusive time scale estimates using 1000 m^2/s for the eddy diffusivity are decadal, as observed.

While it seems likely that the actual mode water formation process is influenced by the mesoscale, the detailed role of eddy variability is difficult to pin down. The estimate of Speer and Tziperman (1992) for the North Atlantic subtropical mode water formation rate of 15 Sv in annual average is by some measures very high. On the other hand, their procedure is unable to capture the episodic and mesoscale nature of mode water formation, and it is possible that this acts to reduce the net formation.

d. Objectives

In the present paper, we examine the formation process of mode waters in an eddy-resolving model of the South Atlantic. Such a study of course aids in validating our South Atlantic model. In addition, however, the high spatial and temporal resolution of the model make it possible to follow the seasonal evolution of the mode water formation process, as well as to examine the role of the mesoscale variability in the subduction mechanics. In this vein, it is gratifying that the model exhibits reasonable levels of eddy kinetic energy.

The paper is organized as follows. In Section 2, the model configuration and model simulation are described. The third section describes the surface mean circulation and variability produced by the last 5 years of a 34-year long experiment. Section 4 investigates the existence of the mode waters in the model simulation and compares their characteristics

with observed properties. A numerical procedure for estimating the instantaneous detrainment rate is proposed in Section 5. This procedure is applied to the model output to study the formation and subduction of Mode Waters over a seasonal cycle in Section 6. Some comments on eddy effects and interannual variability are made. In Section 7, the sites of mode water formation are described and the paper ends with a discussion and conclusions section.

2. Model simulations

Our South Atlantic simulation used the Sigma-coordinate Primitive Equation Model (SPEM) developed by Haidvogel and collaborators (Haidvogel *et al.,* 1991). This study employs SPEM version 5.1. Modifications of the predecessor SPEM version 3.9 for basin scale simulations has been described in Barnier *et al.* (1998), and its application at coarse resolution to the South Atlantic Basin is presented in Marchesiello *et al.* (1998). Many procedures similar to those described in the above references were used in this study. Nonetheless, several novel modifications have been applied to version 5.1 for this high resolution experiment; these are detailed in de Miranda (1996).

The model horizontal resolution is 0.3° in longitude and 0.3° cos ϕ in latitude (where ϕ is latitude). The model has 20 levels in the vertical. The vertical discretization has been changed to a staggered grid; i.e., the vertical velocity points fall between the tracer (temperature, salinity) points, as in the classical C-grid. The previous topography following vertical coordinate transformation ($\sigma = 1 + 2\, z/h(x, y)$ where h is the depth of bottom topography) has been changed to a more general formulation allowing vertical stretching (Song and Haidvogel, 1993):

$$z = h_c\sigma + (h - h_c)C(\sigma) \tag{1}$$

where

$$C(\sigma) = (1 - \gamma)P_\theta(\sigma) + \gamma R_\theta(\sigma)$$

with:

$$P_\theta(\sigma) = \frac{\sinh(\theta\sigma)}{\sinh\theta} \quad R_\theta(\sigma) = \frac{\tanh[\theta(\sigma + 0.5)]}{2\tanh(0.5\theta)} - \frac{1}{2}\cdot$$

The quantities θ, γ are parameters which have been set to 5 and 0.4, respectively. The quantity h_c is the minimum allowed ocean depth (200 m). Table 1 shows the vertical resolution for various total depths.

The bottom topography has been smoothed (see Fig. 1) following the criteria defined by Barnier *et al.* (1998) to minimize hydrostatic inconsistency and, thus, the pressure gradient error inherent in the sigma coordinate formulation (Beckmann and Haidvogel, 1993). Algorithms for open boundary conditions (Barnier *et al.,* 1998) have been successfully used in low resolution simulations and have been updated for this version of the high

Table 1. Depths of the vertical velocity points for various total depths. Model levels are labeled from 0 to 20 from bottom to surface.

Level	Ω Points for $h = 200$ m	Ω Points for $h = 2850$ m	Ω Points for $h = 5500$ m	T Points for $h = 5500$ m
20	0.00	0.00	0.00	−14.42
19	−10.00	−20.03	−30.05	−47.29
18	−20.00	−43.30	−66.60	−88.55
17	−30.00	−71.92	−113.84	−143.30
16	−40.00	−108.94	−177.89	−218.78
15	−50.00	−158.64	−267.27	−324.83
14	−60.00	−226.50	−393.01	−473.34
13	−70.00	−318.60	−567.19	−675.59
12	−80.00	−439.47	−798.94	−936.84
11	−90.00	−588.95	−1087.91	−1249.77
10	−100.00	−759.64	−1419.28	−1592.85
9	−110.00	−938.48	−1766.95	−1938.62
8	−120.00	−1112.90	−2105.81	−2267.60
7	−130.00	−1277.09	−2424.19	−2576.74
6	−140.00	−1433.59	−2727.18	−2877.99
5	−150.00	−1591.00	−3032.00	−3192.27
4	−160.00	−1761.00	−3361.99	−3544.51
3	−170.00	−1956.64	−3743.28	−3961.95
2	−180.00	−2192.18	−4204.35	−4474.63
1	−190.00	−2483.64	−4777.29	−5117.25
0	−200.00	−2850.00	−5500.00	

resolution numerical model. Tracers and baroclinic velocities needed at boundary points for inflow conditions are estimated from the climatology of Levitus (1982) and thermal wind. A total eastward volume transport of 140 Sv is imposed at the Drake Passage and across the eastern boundary (south of Africa) at 30E. The zonally and vertically averaged transport vanishes between America and Africa at 16S (see Fig. 1). The model is initialized with a 20 Sv southward inflow in the Western Boundary Current at the northern open boundary, a 70 Sv westward inflow in the Agulhas Current offshore of the South African coast and a 10 Sv westward inflow along Antarctica at the eastern boundary.

The model was integrated for 34 model years. For the first 19 years, Laplacian diffusion and viscosity acting along true horizontal were used (Barnier *et al.,* 1998). The eddy coefficients varied linearly with the inverse of the grid size. Maximum values were 75 $m^2\ s^{-1}$ and 150 $m^2\ s^{-1}$ for viscosity and diffusivity, respectively. For the last 15 years a biharmonic horizontal operator was used (Beckmann, personal communication). The respective eddy coefficient varied as the third power of the grid size; a maximum value of $2.5 \times 10^{11}\ m^4\ s^{-1}$ occurred at 16S. The vertical viscosity coefficient is constant and equal to $10^{-3}\ m^2\ s^{-1}$, and the vertical diffusion coefficient is a function of the stratification: $A_v = a_0/N$ where N is the Brunt-Väisälä frequency and $a_0 = 10^{-7}\ m^2\ s^{-2}$ (Cummins *et al.,* 1990). The model used implicit vertical diffusion as a model of mixed layer convection; i.e.,

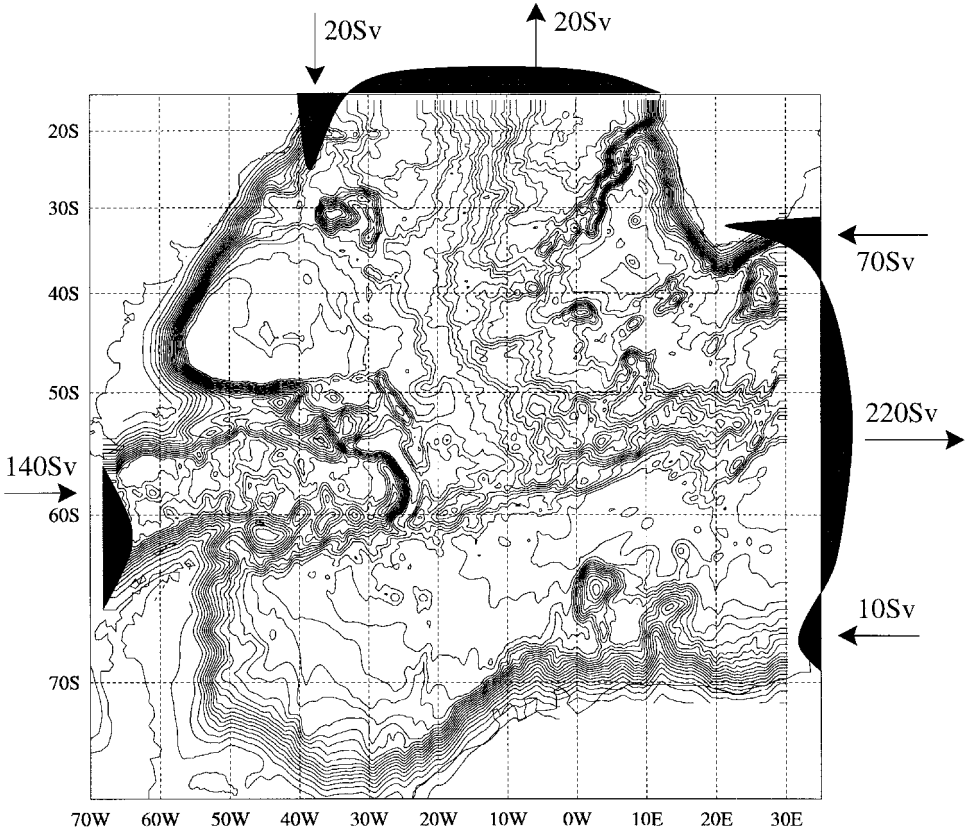

Figure 1. Smoothed bottom topography (in meters) of the South Atlantic used for our numerical simulations. Also shown is a schematic representation of the barotropic transports maintained at each open model boundary. CI: 1000 meters.

hydrostatic stability is tested at each time step, and a large value ($a_0 = 0.5\ m^2\ s^{-2}$) is assigned to the vertical diffusion coefficient in case of instability. In addition, perfect mixing via convective adjustment was done every 10 time steps (3 hours) at locations of hydrostatic instability.

The model is started from rest in January (austral summer), and initialized in temperature and salinity from climatology (Levitus, 1982). The model is driven by seasonally varying wind fields derived from ECMWF forecasts for years 1986 to 1988 (Siefridt, 1994). Monthly mean values were linearly interpolated to each time step. The surface heat flux forcing was taken from Barnier *et al.* (1995), which is based on ECMWF monthly-mean climatologies from years 1986 to 1988. Salinity forcing occurs via relaxation toward climatological surface salinity (Levitus, 1982), using the relaxation time proposed by Barnier *et al.* (1995) for temperature. All surface fluxes of momentum, heat and salinity were distributed uniformly throughout the upper 50 meters. Sea ice was parameterized

using a strong relaxation toward Levitus salinity and temperature was relaxed to the sea ice freezing point at locations where the ECMWF sea surface temperature was lower than −2°C.

3. Upper ocean circulation

The global mean circulation produced by the model simulation is described in de Miranda (1996). We briefly discuss here the upper ocean mean circulation and variability, compare them to South Atlantic observations and emphasize the parts relevant to mode waters.

a. Mean surface circulation

We present in Figure 2 the annual mean salinity at 200 meters with positions of Antarctic Circumpolar Current (ACC) fronts, both as computed by the model, superimposed. We will argue shortly the model fronts correspond to observed ACC fronts. In Figure 3, we show the annual mean temperature at 200 meters with vectors representing velocities averaged over the upper 200 meters, again as computed by the model.

The ACC brings freshwater from the Pacific Ocean through the Drake Passage and from polar regions. In the Confluence Region where the eddy activity is very intense (as confirmed below) these cold and fresh waters are mixed with warm and saline waters coming from the subtropical gyre and advected southward by the Brazil Current. The recirculation of the Brazil Current appears in the western subtropical gyre.

The model Agulhas Current flows poleward along the eastern coast of South Africa (at 30E) and brings warm and saline Indian waters to the South Atlantic. These waters are then advected northwestward by the Benguela Current and the eastern branch of the subtropical gyre. The retroflection of the Agulhas Current is seen, as is the Benguela upwelling on the western coast of Africa. The latter is particularly evident in the low salinities and cool temperatures characteristic of this area.

Other Southern Ocean circulation patterns appear in the circulation as well. The Weddell Sea has a strong cyclonic circulation, the northern branch of which coincides with the southern flank of the ACC. A strong anticyclonic circulation occurs at 45W and 45S the location of a deep topographic feature known as the Zapiola Drift. This circulation appears in hydrographic measurements (Saunders and King, 1995a,b), current meters (Weatherly, 1993), has some theoretical foundation (Dewar, 1998) and is discussed in the context of this model simulation in de Miranda *et al.* (1999). The Zapiola Drift is also particularly evident in trajectories of subsurface floats (Ollitrault, 1998).

The positions of the major fronts (Fig. 2) are determined using classical definitions (Peterson and Whitworth, 1989). The model frontal positions are in good agreement with those positions determined from hydrographic measurements at the Greenwich Meridian (Whitworth and Nowlin, 1987) and in the western South Atlantic (Peterson and Whitworth, 1989).

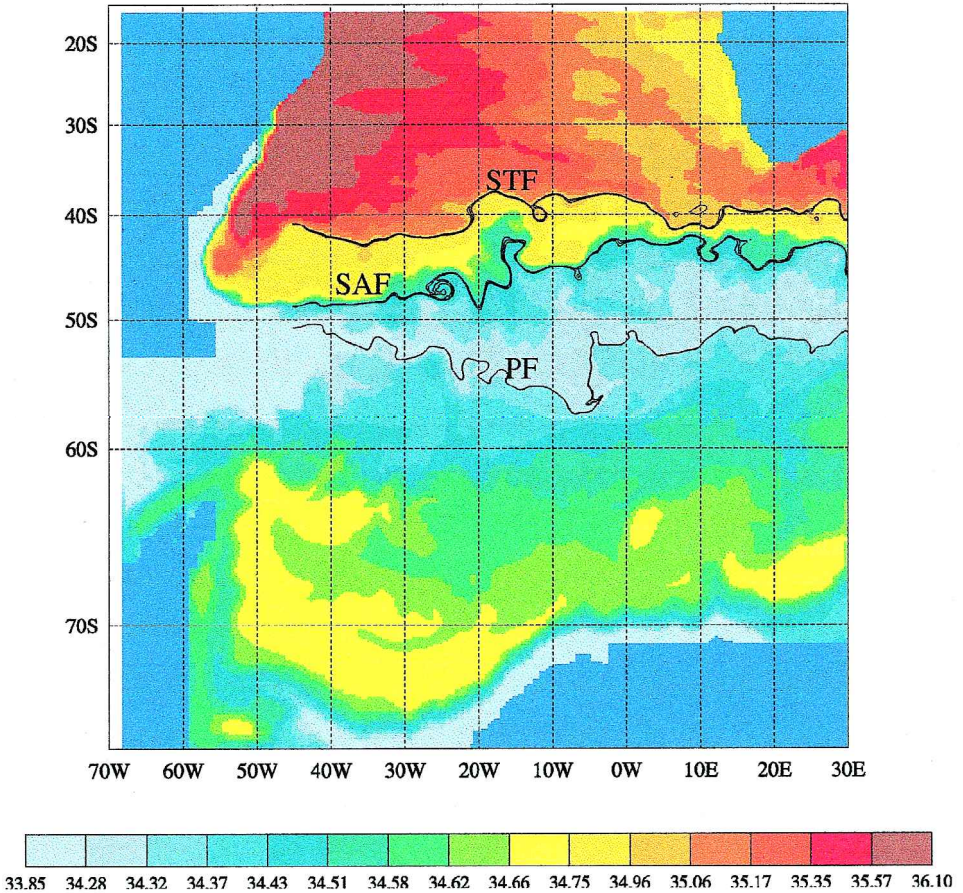

Figure 2. Mean annual salinity (year 33) at 200 m and position of fronts. From north to south: Subtropical Front (S = 35. at 200 m), Subantarctic Front (S = 34.5 at 200 m) and Polar Front (2°C at 200 m).

In summary, the mean kinematic and hydrographic structure of the South Atlantic and the Antarctic Circumpolar Current is well represented in the model.

b. Seasonal variability

The model reproduces a seasonal cycle, with the formation of a seasonal pycnocline in summer and its subsequent degradation by surface cooling in winter. In the subtropical gyre, outcropping regions of density layers move poleward in summer as the seasonal mixed layer forms (Fig. 4). The outcropping window which corresponds to the density of mode waters (σ_0 between 25.7 and 26.5) is then located between 48S and 38S. In winter, this window moves equatorward by more than 800 km, and is found between 30S and 40S.

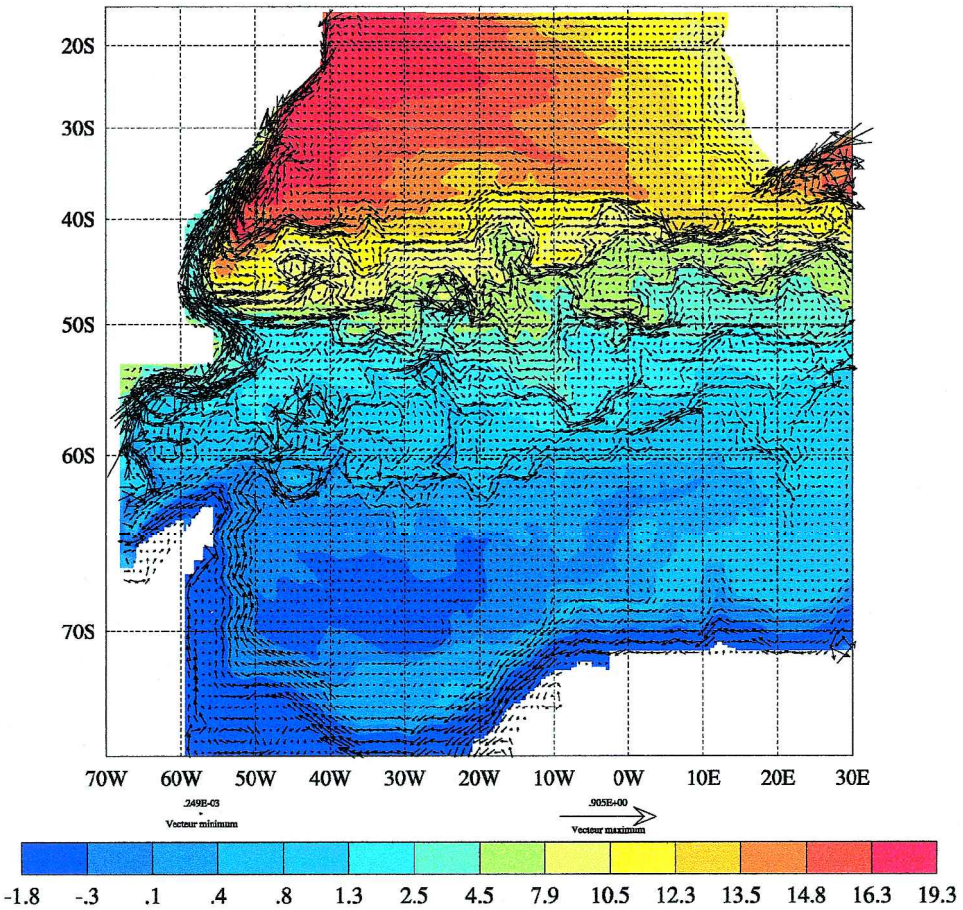

Figure 3. Mean annual temperature (in °C) at 200 meters (year 33) and velocities (in m/s) averaged over the first 200 meters. Only 1 velocity vector over 4 has been plotted. Maximum velocity is 90 cm/s.

In the following, mixed layer depth is defined as the depth of the last model level where density matches the surface density. This definition, which assumes that the mixed layer is the layer over which convective adjustment is performed, yields shallower mixed layers than the more standard definition used in numerical models of the depth where the model density has increased by the amount 0.01 kg/m^3. However, our definition is consistent with the mixed layer parameterization of the model and is why it has been retained.

The mixed layer in late winter exhibits three regions of significant convection (Fig. 5). One is in the southwestern part of the Weddell Sea, where the mixed layer depth reaches more than 2000 meters. Another region of deep convection occurs in the eastern part of the Weddell Sea just south of the Southwest Indian Ridge. We won't analyze these regions of convection as they occur under sea ice and our parameterization of sea ice is very crude.

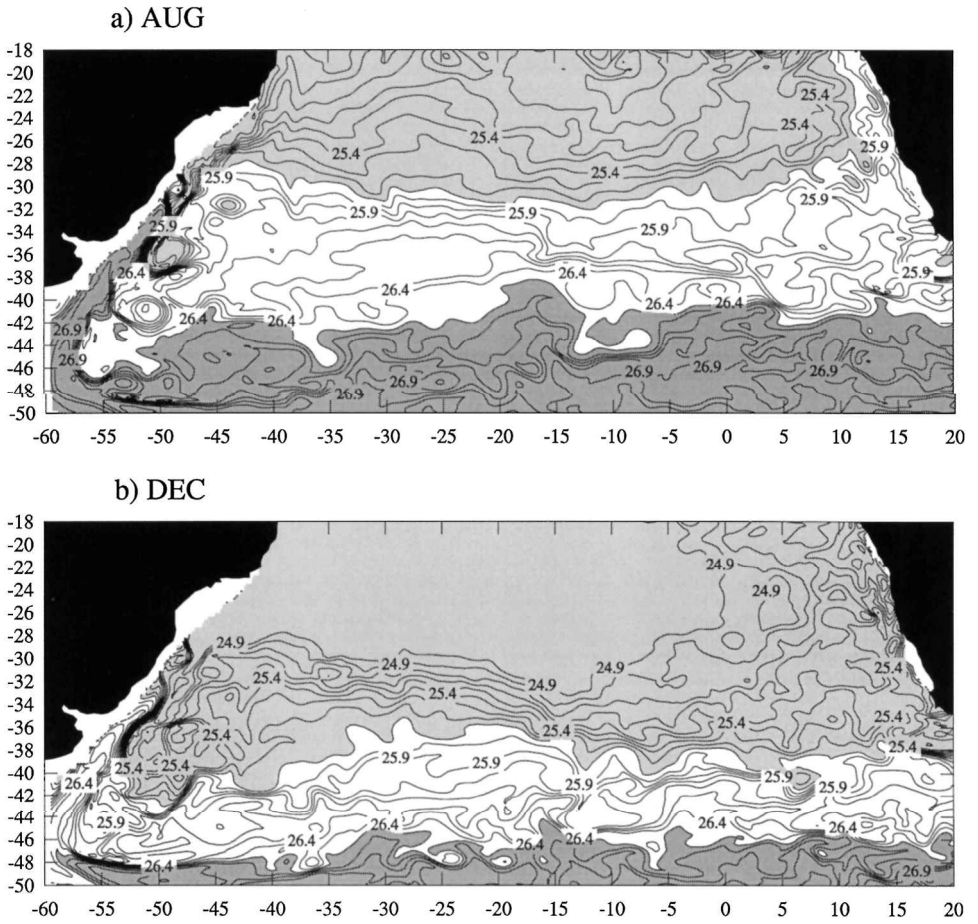

Figure 4. Mixed layer density: (a) at the end of winter 34 (August), (b) at the beginning of summer 34–35 (December, year 34). The clear zone denotes the densities of South Atlantic mode water. CI: 0.1.

The third region of convection is concentrated mostly in the western part of the subtropical gyre, where the mixed layer depth is generally greater than 150 meters. Occasionally, the mixed layer reaches more than 500 meters in the core of eddies located in the Confluence region. The South Atlantic Subtropical Front is located roughly at 40S, and therefore, this window of deep mixed layers in the Argentine Basin occurs in the region where the mean annual surface densities of both the subtropical and subantarctic mode waters are found.

c. Mesoscale activity

To illustrate the eddy activity produced by the model, we present in Figure 6a the eddy kinetic energy averaged over the last 5 years of integration; i.e., years 30 to 34. EKE as

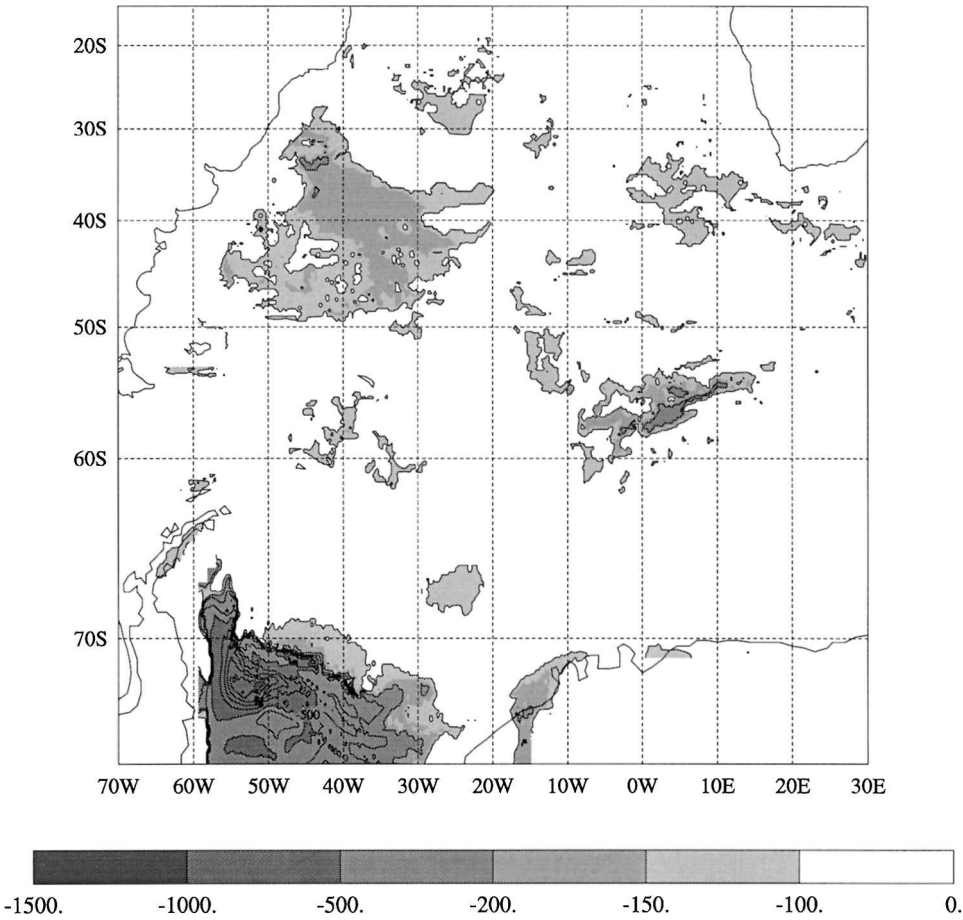

Figure 5. Mixed layer depth (in meters) averaged over winter of the 34th year of integration. CI: 100 meters.

computed from the combined Topex/Poseidon and ERS-1 sea surface height data appears in Figure 6b. The eddy kinetic energy (EKE) reaches more than 2000 $cm^2\ s^{-2}$ in a large region offshore of the Confluence region. These amplitudes are similar to those observed in other high resolution numerical simulations of the North Atlantic (Tréguier, 1992), and are comparable to EKE levels deduced from satellite observations. The levels also support the idea that the Confluence region might be the most eddy energetic region in the world ocean.

The eddy kinetic energy level reached in the model Agulhas retroflection region is clearly underestimated, as can be seen by comparing panels (a) and (b) in Figure 6. This is due to the proximity of the eastern open boundary to the area and the difficulty in representing the Agulhas Current inflow using Levitus data. Both factors mute the natural instability processes of the area.

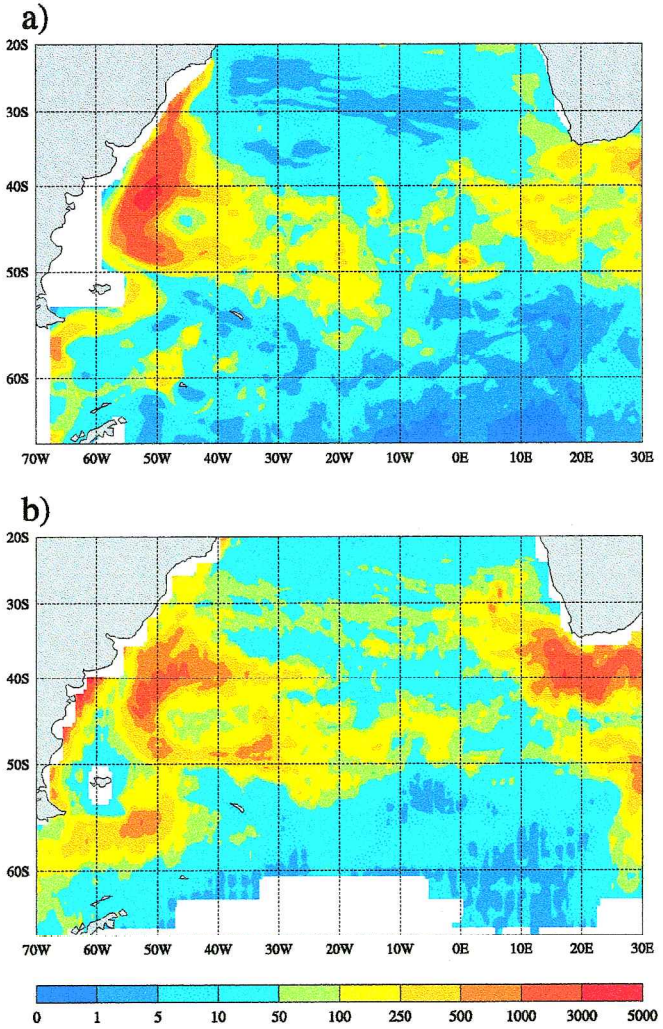

Figure 6. (a) Model Surface Eddy Kinetic Energy averaged over 5 years of integration, (b) Eddy kinetic Energy estimated from the combined Topex-Poseidon and ERS-1 altimetric signal (Ducet and Le Traon, personal communication). Units are cm^2s^{-2}.

4. Mode waters in the numerical simulation

For the purposes of analyzing the model mode waters, we have examined the last 5 years of the 34-year long simulation. Several thermostads are found in the upper thermocline in the subtropical gyre, as shown in the vertical-meridional sections of potential temperature at 40W (Fig. 7) and at 25W (Fig. 8).

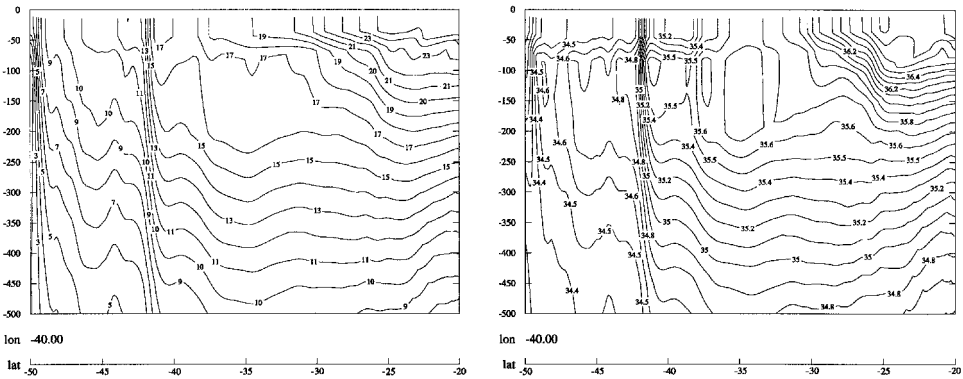

Figure 7. Temperature (°C) and salinity along a north-south section at 40W in December (model year 34).

At 40W we find two distinct thermostads. One is located just north of the Subtropical Front (identified as the strong temperature front at 41S) and is made of waters with temperatures between 15°C and 17°C. This thermostad covers the depth range from 70 to 240 m and extends into the subtropical gyre by more than 10° in latitude (to 29S). The waters are relatively salty ($35.5 < S < 35.7$) but light ($26.1 < \sigma_0 < 26.3$), and correspond to the subtropical mode waters (STMW) found by Provost *et al.* (1995).

Another thermostad with temperatures ranging between 9°C and 11°C is found north of the Subantarctic Front (identified as the strong temperature front at 49S), in the depth range of 50 to 240 m. The waters are relatively fresh ($34.7 < S < 34.8$) and dense ($26.6 < \sigma_0 < 26.7$) and correspond to the SAMW of McCartney (1982).

Farther east, at 25W (Fig. 8) the Subtropical Front ($S = 34.9$ at 200 m) is located at 43S and the Subantarctic Front (4°C at 200 m) at 48S. The shallow subsurface front at 38S is formed by a meander of the STF. We distinguish three thermostads. The first one of temperature 14°C is found in the subtropical gyre north of 38S. The water properties,

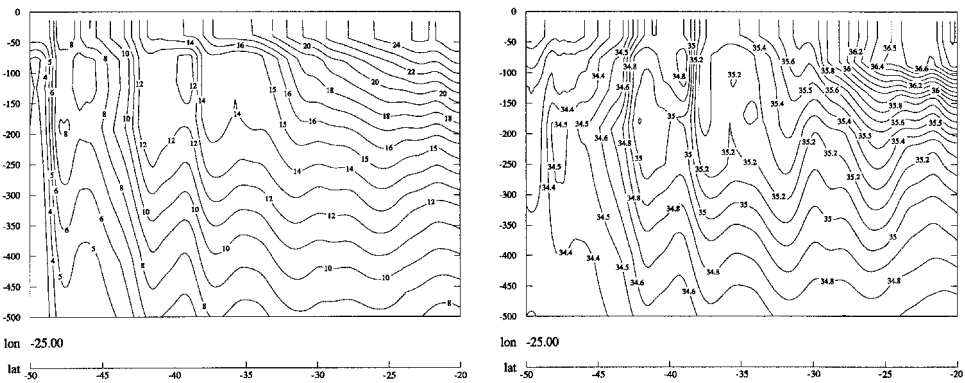

Figure 8. Temperature (°C) and salinity along a north-south section at 25W in December (model year 34).

relatively high salinity ($35.2 < S < 35.3$) and light density ($26.2 < \sigma_0 < 26.3$) are characteristics of subtropical waters. The water is thus identified as STMW, although it is slightly cooler than that found more to the west.

The other thermostad with temperatures between 12 and 13°C is found at 40S; i.e., still to the north of the STF, and is made of saline waters with salinity of 35 or more. Therefore, this is STMW, but some characteristics are more similar to McCartney's SAMW. The water density is $26.4 < \sigma_0 < 26.5$. The southernmost thermostad found between the SAF and the STF is composed of cold and fresh water (7–8°C, $\sigma_0 = 26.8$–27, $S = 34.2$–34.3) typical of subantarctic origin.

From these two sections at 40W and 25W, it appears that mode waters get cooler and denser eastward, reflecting the northeast orientation of the outcropping line in late winter (Fig. 4). The latter is a direct consequence of mixing between subtropical and subantarctic waters all along the ACC path.

Two types of mode waters can clearly be identified based on salinity within the model. Pycnostads of water more saline than 35 are subtropical mode waters, while those fresher than 35 are subantarctic mode water. This is in agreement with observational characterizations of South Atlantic mode waters, suggesting that the model captures the essential mode water dynamics.

5. Entrainment—Detrainment

a. Fundamentals

The strong thermostads discussed above were not present in the initial conditions, and therefore are the combined result of the buoyancy forcing and the thermocline ventilation dynamics. The former exhibits a seasonal cycle which may have a role to play.

Ventilation dynamics and the processes by which subsurface densities are replenished has been the subject of past study. Surface water can enter the pycnocline in a subtropical gyre either via Ekman pumping or lateral induction, the latter involving "horizontal" flow across a sloping mixed layer base. Subsequent evolution is largely conservative. In a subpolar gyre, fluid can upwell from the seasonal pycnocline into the mixed layer, where atmospheric contact modifies its properties. These processes are routinely referred to in the literature as "detrainment," denoting the mass flux which leaves the mixed layer through its base, and "entrainment," denoting the mass flux that enters the mixed layer from the pycnocline.

The general circulation advects freshly detrained water within the gyre. Whether this water actually remains subducted involves its subsequent interactions with the seasonal pycnocline. Thus water detrained at a given location can be entrained during mixed layer deepening at a different position and during a different winter, as illustrated in Figure 9. Of course, some water is quasi-permanently subducted and becomes the water responsible for stratifying the upper ocean.

At a given location, the seasonal cycle of the mixed layer can thus be divided into three phases (Fig. 9):

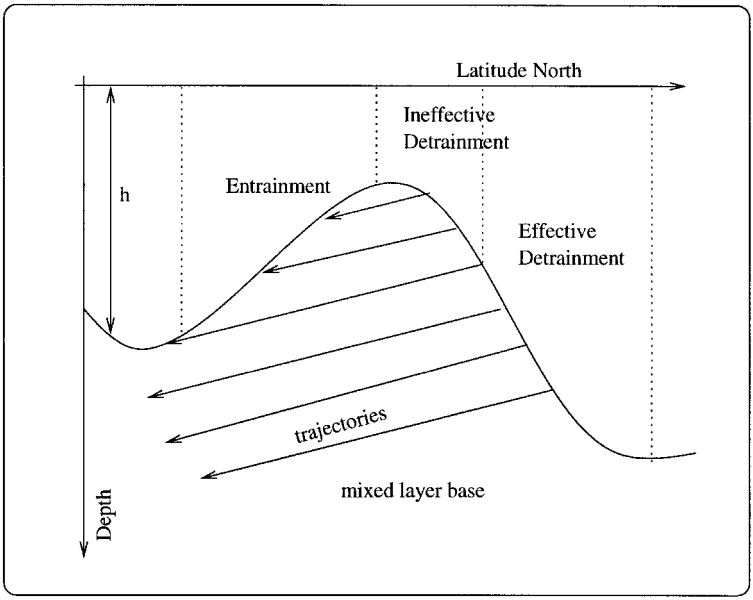

Figure 9. Trajectories of subducted water: water which leaves the mixed layer at a given location can be entrained downstream.

- the mixed layer shallows, leaving water behind. This phase is called the effective detrainment phase,
- the mixed layer shallows, but water left behind is overtaken later in the mixed layer at another location: this is the ineffective detrainment phase,
- the mixed layer deepens overtaking water pumped downward upstream: this is the entrainment phase.

As opposed to the above essentially Eulerian view, we compute annual mean subduction rates as a function of density using a "pseudo-Lagrangian" approach; i.e., the calculation follows the density layers as they move with the seasonal cycle and eddy variability. This differs from a purely Lagrangian approach, which follows fluid parcels. Rather, density outcrops are followed and mass flux across the mixed layer base is estimated. We choose this procedure given our interest in the specific density ranges associated with mode waters. Over the course of a year, both entrainment and detrainment occur. However, if density surfaces are followed, the result of the subduction process is the net effective subduction; i.e., the total mass flux in that density class which, over a year, leaves the mixed layer and is not entrained elsewhere in the gyre. This measures the amount of water which has gone irreversibly from the mixed layer to the main thermocline, thereby increasing the amount of water contained in the main thermocline in a density class. One should expect that this number can be very small compared to instantaneous subduction

rates. The result is algebraic, it can be either positive or negative depending on the balance between formation and destruction at the base of the mixed layer within each density class. We will abusively use the word subduction to describe our calculation, without distinction between obduction and subduction.

The calculation of this subduction rate requires very accurate information about the mixed layer and submixed layer currents. Such information is not usually available from field observations, and certainly not from the usual hydrographic measurements. The considerable spatial and temporal resolution of our numerical model, however, allows us to quantify this process. But since our model is not a continuous model, but a grid point model, we evaluated this subduction rate in the finite differences scheme of the model in the most accurate way. A formulaic description of our procedure follows.

b. Instantaneous subduction rate

The instantaneous subduction rate D_e over a region of the ocean is defined as the mass flux leaving the mixed layer at a given time (Cushman-Roisin, 1987b):

$$D_e = \iint_{s_b} d_e \cdot dA \tag{2}$$

where

$$d_e = -(w + u \cdot h_x + v \cdot h_y + h_t). \tag{3}$$

Subscripts x, y, t denote derivatives according to longitude (x), latitude (y) and time (t); u, v and w are the usual three velocity components; s_b is the ocean surface area enclosing the region of interest; dA is an area element and h is the thickness of the mixed layer (see Fig. 10). In the following we shall use $\mathbf{u}_H$ for the horizontal velocity vector. The result is a net subduction rate calculated for each density class, it does not differentiate obduction and subduction.

The above equation for instantaneous subduction is evaluated between two isopycnals, ρ_1 and ρ_2, as shown schematically in Figure 10. Because of the "pseudo-Lagrangian" formulation, the contribution of diapycnal mixing to the subduction rate is implicitly accounted for. Moreover, this contribution is small as the diapycnal mixing in the mixed layer is performed by a biharmonic horizontal diffusion with a small coefficient.

The numerical model calculates vertical velocity w by a vertical integration of the continuity equation. While correct in theory, in practice this gives a rather noisy w field, which if used directly in Eq. 3 would corrupt the computation. Instead, we used the continuity equation integrated over the volume between the two isopycnals to replace w in the subduction calculation. This yields to the finite difference representation of Eq. 2 (see Appendix):

$$D_e = -\sum_{n=1}^{nboxes} h_t(n)\, dA(n) - \sum_{n=1}^{nboxes} \mathbf{u} \cdot \mathbf{n}\, ds_l(n) \tag{4}$$

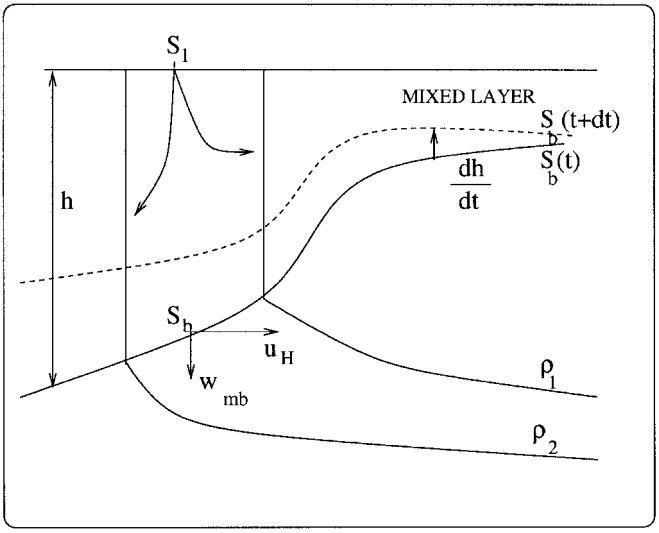

Figure 10. Diagram of the mixed layer notation used in the calculation of the subduction rate.

where the boxes are the model grid boxes, dA is the surface area of a grid box, s_l the lateral surface defined by our chosen densities and **n** the local normal to the surface s_l. The model output allows for a straightforward evaluation of the resulting formula. We have computed the instantaneous subduction rate using archived model snapshots at three days intervals from the last 5 years of the simulation. Without convection, the base of the mixed layer is the depth over which the body-force is applied, i.e., roughly 50 m (de Miranda, 1996). Otherwise, the mixed layer depth was computed as described in Section 3. Several density ranges have been considered.

The instantaneous subduction rate is plotted as a function of time during model year 33 for various density ranges (Fig. 11). The contribution of the vertical motion of the mixed layer depth (the h_t term in Eq. 4) to the subduction rate is also plotted for density classes from 26.1 to 26.5 (Fig. 11a).

For the density classes between 26.5 and 26.9 (Fig. 11b) we added the volume flux at the base of the "body-force" layer due to Ekman pumping. In summer, the Ekman pumping and the subduction rate have similar amplitude, but there are differences which reflect that the Ekman pumping is not the only responsible factor of subduction (see Eq. 3). For densities greater than 26.6, the negative detrainment observed in summer is the reflection of negative Ekman pumping (upwelling) in these density layers. In winter the Ekman pumping is not responsible for the mass flux through the base of the mixed layer. This is not a surprise in winter as the base of the "body-force" layer is not the base of the mixed layer as soon as cooling forces convection.

The subduction rates of the layers shown in Figure 11 present similarities and significant differences (Fig. 11). All the density ranges show entrainment (negative subduction rate) when the mixed layer deepens in fall (in May, starting at day 11640) in response to strong

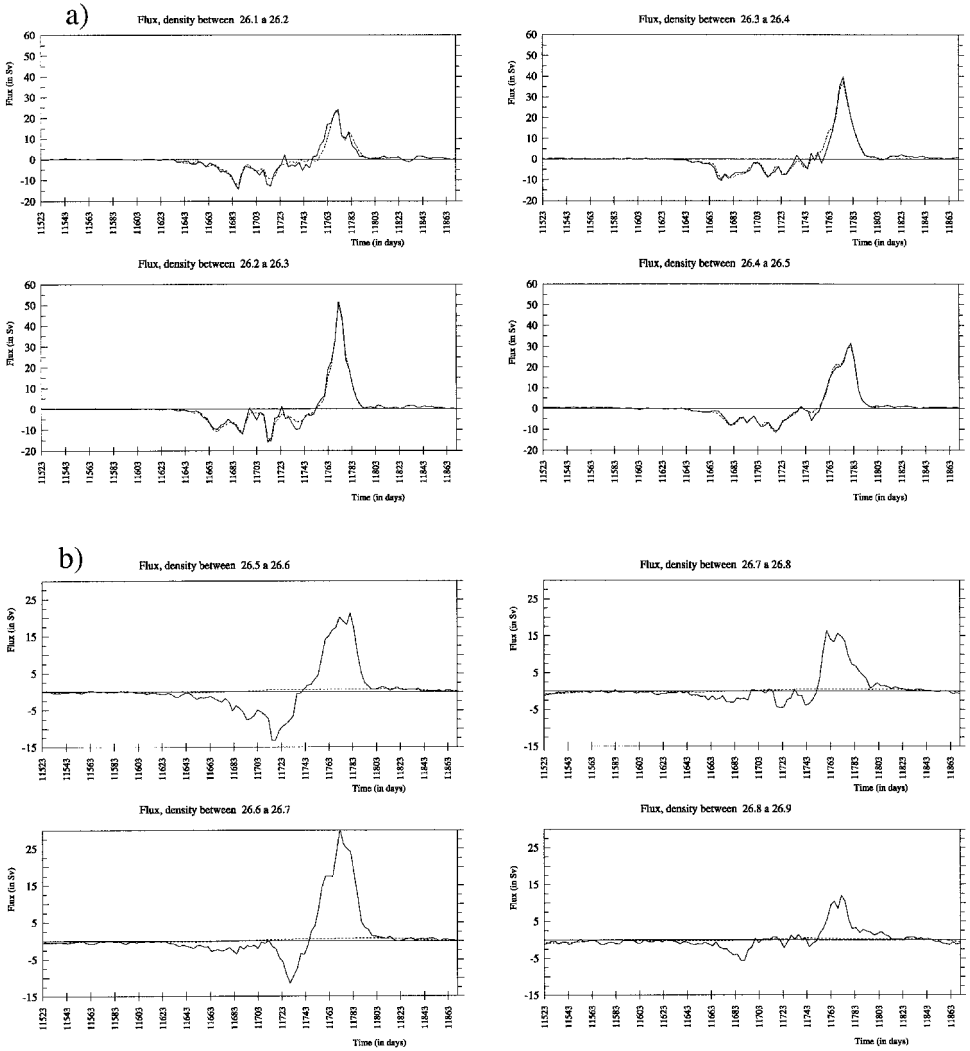

Figure 11. Instantaneous subduction rate as a function of time during model year 33 for different density classes between 26.1 and 26.9: (a) 4 density classes between 26.1 and 26.4. The solid line is the subduction rate (in Sv) and the dashed line is the flux (in Sv) due to Ekman pumping. (b) Four density classes between 26.5 and 26.9. The solid line is the subduction rate (in Sv) and the dashed line is the contribution of $\partial h/\partial t$; i.e., the first term in the subduction calculation. Time is given in days and the first day is January, 1st. The first day of spring (September 1 in the southern hemisphere) is day 11761.

cooling by the atmosphere. This is followed by a short, but intense, detrainment phase at the end of winter or early spring.

In fall, at the start of cooling, the mixed layer deepens and $-\partial h/\partial t$ is negative. This is the entrainment phase where water below the mixed layer enters the mixed layer. This period is

marked by significant variability in the 10 to 30 day band. Large bursts of subduction rate indicate energetic eddy variability.

In late winter, the mixed layer rapidly shallows, producing a maximum subduction rate in early spring (roughly around day 11760). This is consistent with the general idea that subduction is maximum in early spring (Stommel, 1979). A maximum instantaneous subduction of 50 Sv is reached for the density range of 26.2–26.3, which corresponds to the 15–17°C STMW.

During the summer months (the end of the calendar year), the contribution of $\partial h/\partial t$ essentially vanishes, because the stratification is stable and the mixed layer remains constant at the depth over which the body-force is distributed (50 m). The subduction rate, however, does not vanish; rather, a small detrainment (less than 1 Sv) is maintained by Ekman pumping and eddies, the latter being indicated by the variability.

In all the results in Figure 11b, the contribution of $\partial h/\partial t$ to the subduction rate is very close to the total D_e, indicating that the vertical migration of the mixed layer base is the dominant factor in the calculation of instantaneous subduction rate.

The 10 to 30 days variability seen in these curves is associated with intense eddy activity. Peaks in subduction rate observed during fall can be associated with strong nonlinear events, such as intense mesoscale eddies, or rapid shallowing of the mixed layer in a region of the outcropping window. The western part of the subtropical gyre is characterized by very strong eddy activity (Fig. 6) whose contribution to instantaneous subduction rate is likely to be important.

The impact of eddies is important in the entrainment phase, and they certainly contribute to precondition the properties of the mixed layer before detrainment occurs. However, during the detrainment phase in early spring, eddies are likely to play a minor role, because the retreat of the mixed layer is very rapid.

6. Annual mean subduction rates

a. Annual subduction rate

The annual mean subduction rate between two density surfaces ρ_1 and ρ_2 (as in Fig. 10) is defined as:

$$S_r = \frac{1}{T}\int_0^T D_e \, dt \tag{5}$$

where $T = 1$ year, and can easily be estimated by averaging in time the instantaneous subduction rate computed in the previous section. Note here that this mean has to take into account the movement of density layers, which mean average the instantaneous subduction rate for each density class separately.

The results for different density ranges in model year 33 are summarized in Table 2. The third column gives the contribution of dh/dt to the complete integration of the mean subduction rate.

Table 2. Annual subduction rate (in Sv) for year 33 in different density classes. The third column represents the contribution of *dh/dt* in the complete integration. Last column represents the renewal rates (in %).

Min. and max. densities	Year mean S_r (10^6 m^3 s^{-1})	*dh/dt* contribution (10^6 m^3 s^{-1})	Renewal rates (in %)
25.70–25.80	0.56	0.15	12.2
25.80–25.90	−0.04	−0.33	−.7
25.90–26.00	0.64	0.21	9.9
26.00–26.10	0.16	−0.14	2.1
26.10–26.20	−0.07	−0.09	−0.8
26.20–26.30	0.50	0.32	4.6
26.30–26.40	0.57	0.48	4.5
26.40–26.50	0.59	0.41	4.2
26.50–26.60	0.38	0.26	2.8
26.60–26.70	1.26	1.38	6.4
26.70–26.80	0.60	0.57	2.6
26.80–26.90	0.15	0.31	0.5

The values of S_r are all of the order of 1 Sv, which is very small compared to the instantaneous rate of 45 Sv reached in late winter within some density ranges (cf., Fig. 11). The order of magnitude of these results is smaller than that found for the North Atlantic with other formulations (Qiu and Huang, 1995; Speer and Tziperman, 1992). However, this might reflect the weaker mode water signature in the South Atlantic compared to the 18°C Mode Water of the North Atlantic. The largest annual subduction values are reached for the density ranges between $\sigma_0 = 26.2$ and $\sigma_0 = 26.8$, which correspond to the thermostads identified above.

Annual replacement percentages have been computed as the ratio of the volume produced in one year (integrating the instantaneous subduction rate) to the annual mean volume for each density class. As can be seen in Table 2 there is good agreement between mean annual subduction rates, S_r, and renewal rates. Values of 4 to 6% found for our model mode waters are smaller than those estimated in the North Atlantic for 18°C Mode Water (Speer and Tziperman, 1992) but are in keeping with the weaker South Atlantic mode water.

b. Inter-annual variability

Inter-annual variability is observed in the subduction rates (Fig. 12). These changes are either positive or negative, and occur during both entrainment or detrainment. Since the climatological forcing fields do not change from one model year to the next, these changes can only be related to eddy variability. The average of the annual mean subduction rates over the last 5 years of the model run are shown in Table 3, along with standard deviations of the annual means about the 5 year mean, for the various density classes of South Atlantic STMW.

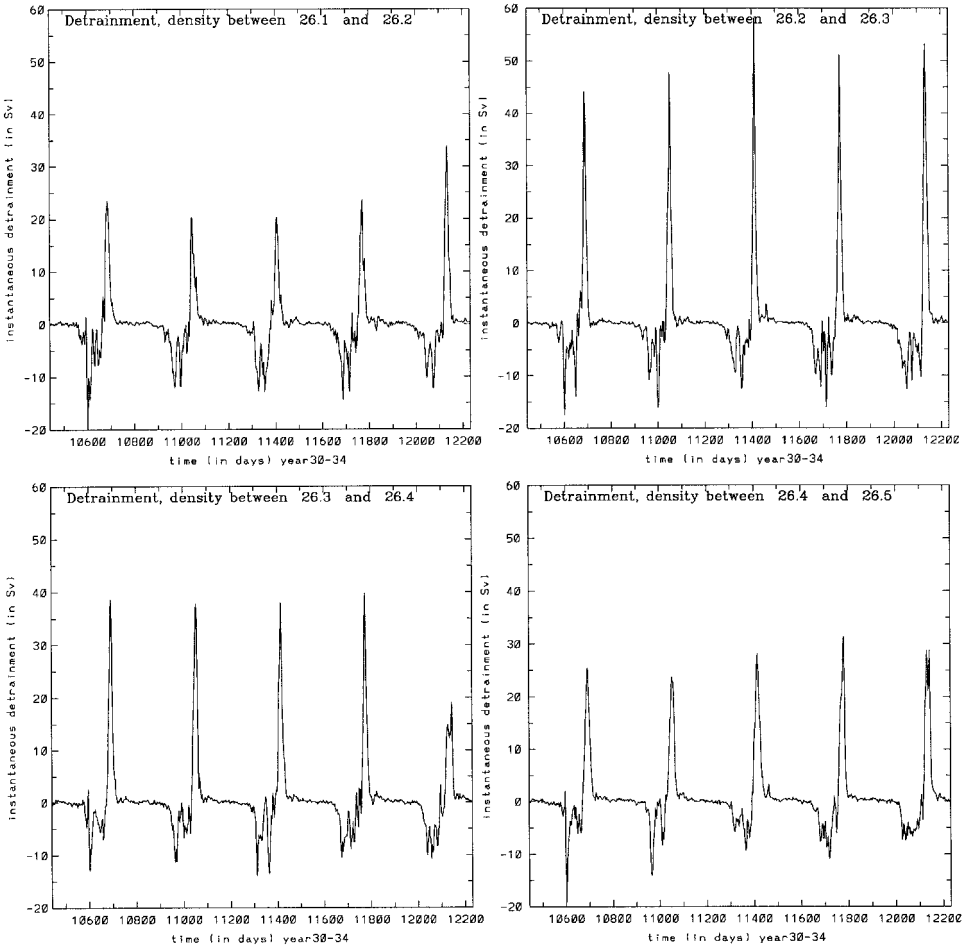

Figure 12. Instantaneous subduction rate for the density range between 26.1 and 26.5, computed from year 30 to 34.

The long-term average supports our conclusions: the largest subduction rates are found for the mode waters identified in the model. Standard deviations are significant but are lower for higher subduction rates. The nonseasonal signal in the subduction rate is very strong and is due to the eddy effects.

c. Volume of density layers

An independent way to investigate water mass formation is to follow in time the variations in volume of given density classes. We have computed the variations of the volume contained between various density surfaces below the mixed layer in order to match in procedure the estimate made above (in Fig. 10, this volume is the one below the mixed layer which is contained between density surfaces ρ_1 and ρ_2). This computation,

Table 3. Five-year mean annual subduction rate (in Sv) for different density classes. The third column is the standard deviation of the annual means about the 5-year mean.

Min. and max. densities	5 years mean S_r (10^6 m^3 s^{-1})	Standard deviation	Water type
25.70–25.80	0.22	*0.28*	
25.80–25.90	0.21	*0.28*	
25.90–26.00	0.24	*0.23*	
26.00–26.10	0.10	*0.18*	
26.10–26.20	−0.03	*0.24*	
26.20–26.30	0.66	*0.14*	STMW
26.30–26.40	0.61	*0.28*	STMW
26.40–26.50	0.72	*0.15*	
26.50–26.60	0.49	*0.18*	
26.60–26.70	0.68	*0.32*	SAMW
26.70–26.80	0.46	*0.16*	SAMW
26.80–26.90	0.26	*0.15*	

made for year 33 is shown in Figure 13. It includes the contribution of all processes involved in volume evolution, such as diffusion across isopycnal surfaces, fluxes through the northern and eastern boundaries (recall boundary data are set on inflow points only), and the flux across the mixed layer.

The contribution of the latter can be independently estimated in cumulating the instantaneous subduction rate at the base of the mixed layer, the mathematical expression of which being $V(t) = \int_0^t D_e(\tau)d\tau$, where $D_e(\tau)$ is the instantaneous subduction rate at instant τ and t is time ($t = 0$ is the beginning of the year). This contribution is reported in Figure 13, with the volume variations for various density layers, and this comparison can be used to validate "*a posteriori*" our calculation of the subduction rate.

For most density layers the volume of density layers (solid lines) regularly decrease because of diapycnal mixing and flux through the open boundaries from the beginning of the year to the end of fall (day 11671). The decrease is fast during the winter due to the deepening of the mixed layer. The detrainment phase, which starts in spring, increases the volume of the layer. The net volume formed during the year is the difference between the volume of water at years end and the volume of water at the beginning of the year. This net volume is very small compared to the volume produced during the detrainment phase of spring, due to the loss of water over the year by diapycnal mixing. This also suggests the model is close to thermodynamic equilibrium in these layers, as aside from interannual variability, the net volume created over a year should vanish.

The comparison with the estimation based on D_e (Fig. 13, dashed lines) shows a very good correlation between the two estimates. The differences reflect all the processes involved in water mass renewal or destruction which are not ventilation. Diapycnal mixing is of course involved, as are leakages through the boundaries. These processes are dominant in the density layer volume in summer (outside the entrainment-detrainment phase). It is clear that the variations in volume are dominated by entrainment during winter

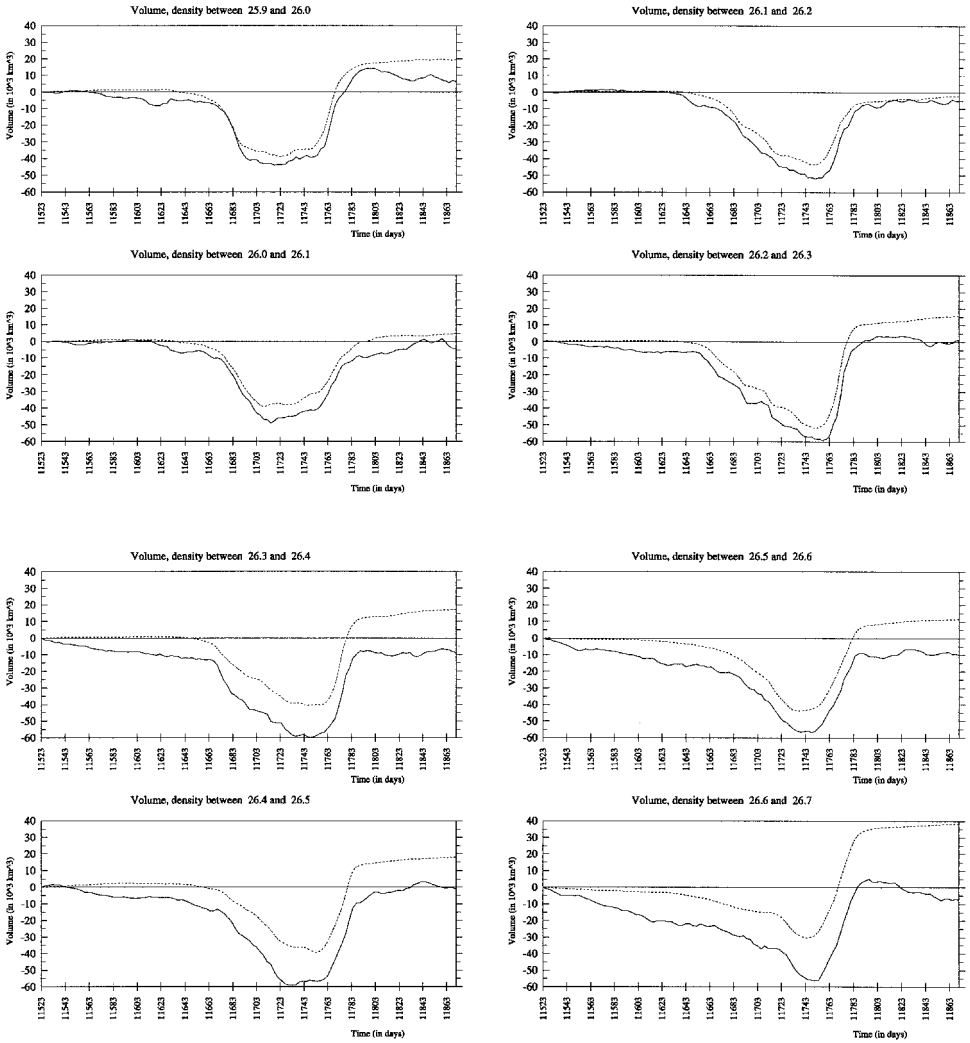

Figure 13. Variations in volume (solid lines) of various density classes between 25.9 and 26.7 during year 33 of the numerical simulation. The dashed lines represent the cumulative total of the volume that went through the mixed layer base since the beginning of the year. Note the sudden volume increase at the end of winter/beginning of spring (around day 11761). Units: 10^3 km^3.

convection, and detrainment in spring when the restratification begins. During these periods, the quantitative agreement between the volume variations and the cumulated volume flux through the mixed layer base is remarkable, which demonstrates the accuracy of our calculation of subduction rate. For the denser density layers (denser than $\sigma_0 = 26.5$) the decreasing slope during winter convection is less pronounced than for lighter waters. This may be a consequence of the more southerly position of these isopycnals, which are

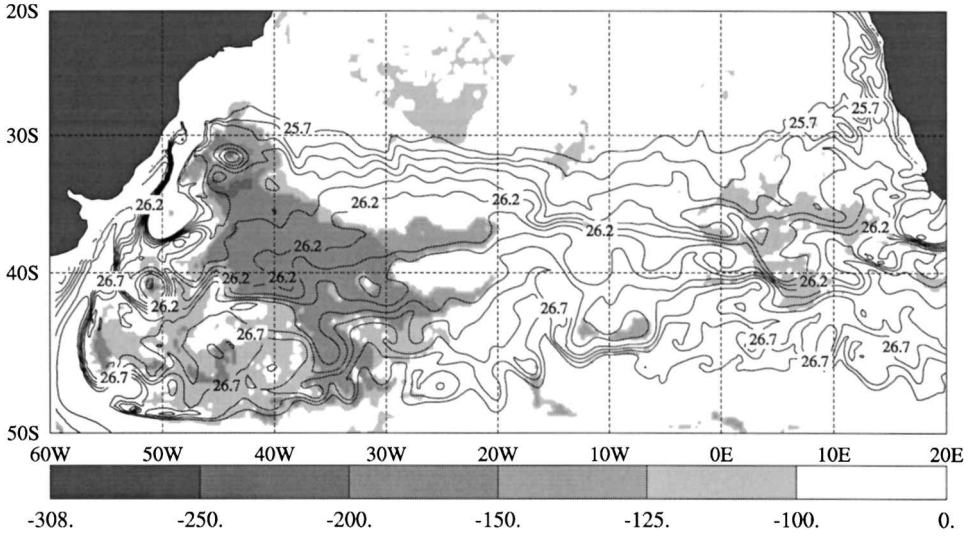

Figure 14. Mixed layer density in August (late winter) of year 34 is contoured. The color scheme denotes mixed layer depth.

south of the region of strong convection (see Fig. 14). The correspondence between these two independent calculations lends credence to them both.

7. Annual cycle of STMW

Interestingly, some of the largest annual subduction rates are found in the density range 26.2 to 26.5, which corresponds to the subtropical mode waters we have identified. In order to clearly identify the region of formation of these mode waters, we investigate the corresponding outcropping region in late winter (late August–early September). This region can be determined by looking at the model depth and density of the mixed layer (Fig. 14).

A large fraction of the region with surface densities from 25.9 to 26.9 obtains a mixed layer thickness greater than 130 m. The majority of this area is occupied by surface densities between 26.0 to 26.3. The winter surface temperatures of this region are between 14 and 16°C which is characteristic of the STMW.

It is interesting that no clear evidence of STMW formation has been found in the Confluence region. There is a deep mixed layer located at 55W and 45S within the density range 26.4–26.5, but it has no physical connection to the pycnostad found at 25W. The turbulence is so strong in the Confluence region that no thermostad found in the winter there can survive and enter the more quiescent subtropical gyre. Nonetheless, the waters exiting the Confluence, while not vertically homogeneous, do form the waters that farther east produce the deep pycnostad of the STMW. We, therefore, suggest the eddies in the Confluence region play a preconditioning role in the development of STMW.

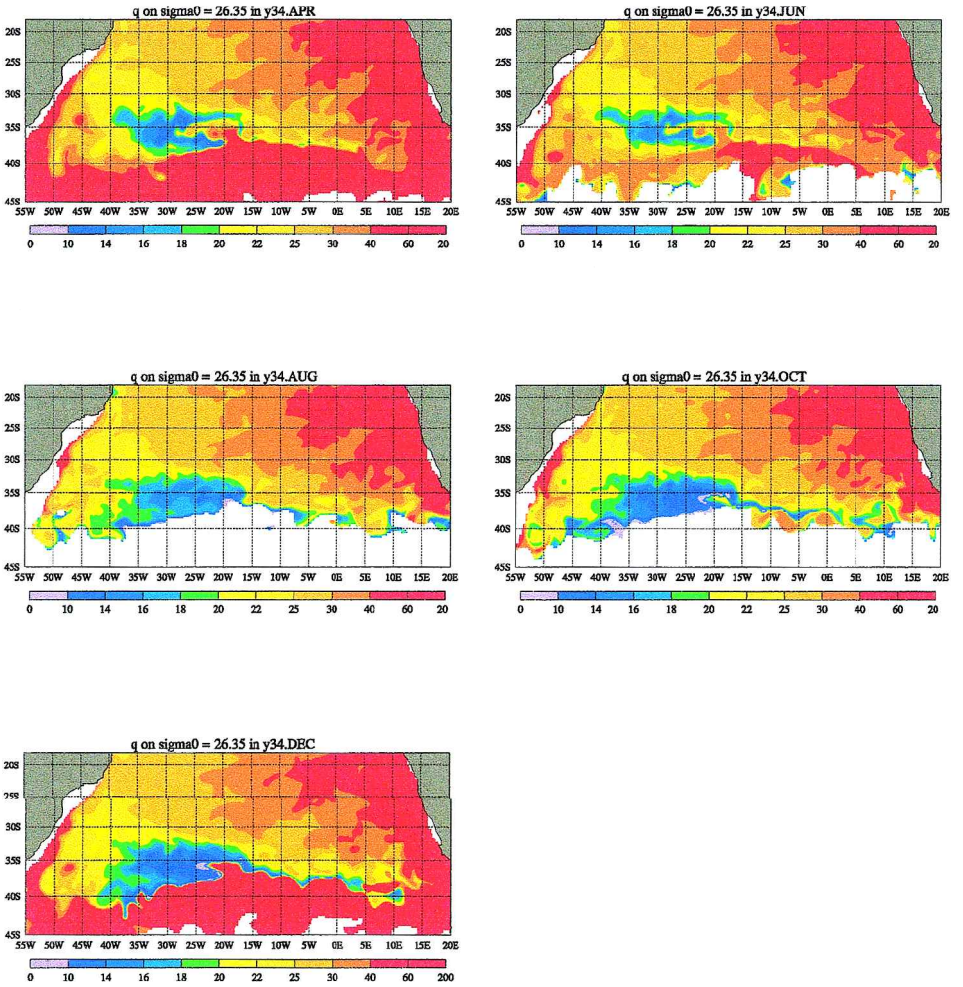

Figure 15. Maps of potential vorticity (year 34) on $\sigma_0 = 26.35$ in April, June, August, October and December. Low potential vorticity (less than 20 10^{-13} $cm^{-1}s^{-1}$) runs from green to purple. The outcrop of the $\sigma_0 = 26.35$ surface is shown by the line. Units are in 10^{-13} $cm^{-1}s^{-1}$.

Given the above subduction rate estimates, which point to mode water formation in the 26.2–26.4 density class, we characterize the formation and distribution cycle by examining the $\sigma_0 = 26.35$ surface. Following McCartney (1977, 1982), we define STMW's as a minimum in large-scale potential vorticity. The distribution of the potential vorticity on the 26.35 surface is shown in Figure 15 for several months of the year.

In April (fall), the $\sigma_0 = 26.35$ outcrop is nearly a zonal line south of 45S. Just north of the outcrop, the seasonal pycnocline appears as a region of high potential vorticity. This is due to the presence of this density class in the late summer mixed layer base. The center of

the subtropical gyre (35S) is a region of low potential vorticity, which is the signature of STMW from previous years. This potential vorticity signal stretches from 40W to 17W.

As winter comes on in June, the surface cooling of this density is reflected in the northward migration of the outcrop. The low potential vorticity region has been slightly reduced in area and has drifted to the northwest. We also notice low potential vorticity inputs all along the outcrop line at 40S.

In late winter (August), the outcrop contacts the "old" low potential vorticity region at 37S between 45 and 15W, and renews the low potential vorticity signature. To the southwest of the region where the old mode water gets renewed (at 40S, between 35 and 45W), there is also a region where new low potential vorticity water is created. Note that in the Confluence region (west of 40W), low potential vorticity filaments are found. These are the result of stretching by the eddy field and indicate eddy potential vorticity mixing.

In October restratification has started east of 15W. In this region, low potential vorticity waters appear as a filament that follows the position of the outcrop in winter rather than as a pool of water like in the western subtropical gyre. In November, the outcrop line moves rapidly toward high latitudes as the seasonal thermocline builds. During this summer period (see the plot for December) the recently formed STMW's are shielded by the mixed layer base from direct contact with the atmosphere. They are advected by the general circulation and partially mixed with the surrounding waters by eddies and diapycnal diffusion. The large pool of STMW in the western subtropical gyre remains strong, but the filament created in the eastern ACC is rapidly mixed away.

The annual mean velocity field on the $\sigma_0 = 26.35$ surface (Fig. 16) is eastward along the outcrop line. But just north of this eastward flow, in the low potential vorticity pool, the flow is essentially cyclonic. The low potential vorticity water is advected northwestward by the western branch of this cyclonic circulation. This explains the existence of a persistent low potential vorticity region north of the winter outcrop (35S).

8. Conclusion

We have seen that a large surface density range feels strong wintertime convection in the western part of the South Atlantic subtropical gyre. Mode waters found in the subtropical gyre correspond to density ranges feeling the strongest convective processes, as measured by the subduction rate. These mode waters roughly correspond to the STMW found by Provost *et al.* (1995). They are not formed in the Confluence region as suggested by Gordon (1981), but rather along a quasi-zonal line to the north of the Subtropical Front. The wintertime coincidence of maximum mixed layer depths and outcropping densities generates a range of mode waters, each in turn reflecting its generation location. In particular, our model generates a progressively denser set of these mode waters as one moves east across the basin. This general trend agrees with the description given by McCartney (1977).

The formation of mode waters is subject to strong interannual variability, reflecting nonseasonally correlated eddy activity. Other mesoscale roles include potential vorticity

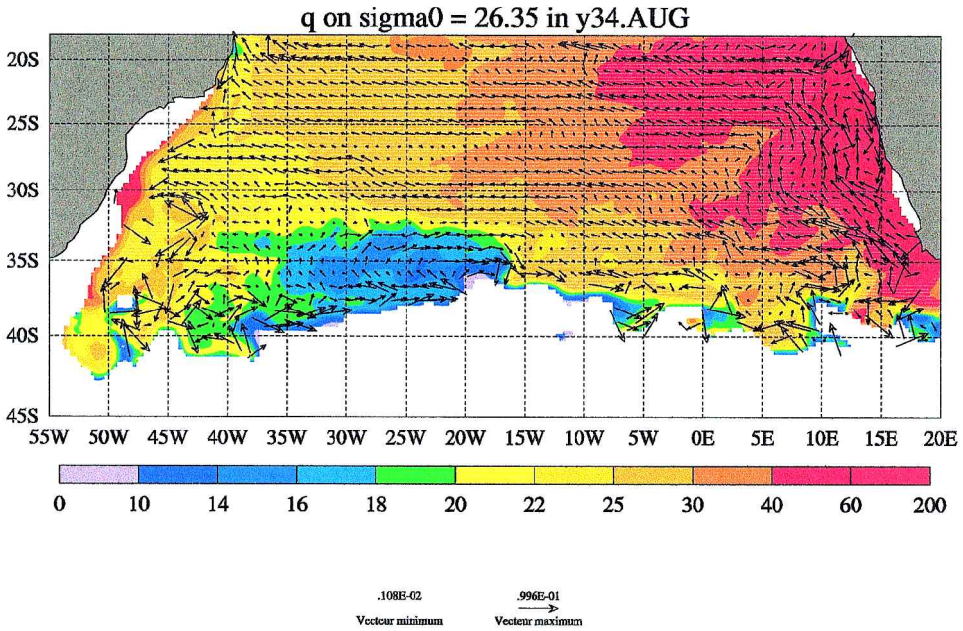

Figure 16. Year 34 annual mean horizontal velocities (in m s^{-1}) and August potential vorticity (in 10^{-13} $cm^{-1}s^{-1}$) on the $\sigma_0 = 26.35$ surface. Velocities in the Confluence region greater than .1 m s^{-1} were not plotted.

mixing in the Confluence region, influencing the properties of the water exiting the Confluence, forcing short term subduction variability and degrading the signature of new mode water via lateral mixing.

Given the model results, we can comment on the theoretical mode water scenarios that have been proposed in the past. This study points strongly at seasonal variability as the principle mechanism renewing mode waters and, as such, differs from the explanation offered in Dewar (1986). There it was suggested the important role of buoyancy flux was in providing a source of low potential vorticity. This signal, although localized in space, was subsequently spread via advection over a larger region of influence. Eddies, parameterized via a down gradient potential vorticity flux, mixed the low potential vorticity water into the gyre, thereby generating a storage mechanism. At no point in this theory is it necessary to explicitly require a seasonal cycle. Cushman-Roisin (1987) also suggested mode waters were to be expected in models without seasonal cycles, although the dynamical role of the buoyancy flux was viewed differently.

The present model shows a considerable erosion of the seasonally generated potential vorticity signal within the subtropical gyre over the course of a year. It is the oncoming winter and associated deep convection which resets a well-mixed column inside the gyre. Thus the explanation offered here of mode waters is that of a local mechanism. This is in some sense reminiscent of the recent work by Joyce and Robbins (1996) for the North

Atlantic mode waters. On the other hand, it is also fair to say the mixed layer dynamics of the present model are crude and that the strong seasonal modulation of the mode water potential vorticity signal hints at an overly diffusive near surface zone. These may favor the importance of local renewal over the more conservative processes inherent in Dewar (1986) and Cushman-Roisin (1987b).

Acknowledgments. The authors, Bernard Barnier and Anne Pimenta de Miranda, were supported by Centre National de la Recherche Scientifique and Ministère de l'Enseignement Supérieur et de la Recherche. Discussions on this topic began between the authors when William K. Dewar was a visiting scientist at LEGI-IMG, during a stay funded by Le Congrès de Mécanique de Grenoble. The hospitality of the LEGI-IMG staff and scientists is gratefully acknowledged. This research was funded by the Institut National des Sciences de l'Univers and IFREMER (Contract IFREMER 96-1-430107) through the Programme National d'Etudes de la Dynamique du Climat as a contribution to WOCE. Support for computations was provided by the Institut du Développement et des Ressources en Informatique Scientifique. The authors are also grateful to (in alphabetical order) Patrick Marchesiello, Jean-Marc Molines and Thong Nguyen for their generous and invaluable help with modeling and computing techniques.

APPENDIX

The instantaneous subduction rate D_e of mass leaving the mixed layer at a given time is defined as Cushman-Roisin (1987):

$$D_e = -\iint_{s_b} d_e \, dA = -\iint_{s_b} (w + u \cdot h_x + v \cdot h_y + h_t) \, dA. \tag{6}$$

Subscripts x, y, t denote derivatives with respect to longitude (x), latitude (y) and time (t); u, v and w are the usual three velocity components; s_b denotes the area of integration, dA the surface area of the outcrop window and h is the mixed layer thickness (see Fig. 10). In the following, we shall use $\mathbf{u}_H$ for the horizontal velocity. Since our model is not a continuous model, but a grid point model, we try below to evaluate D_e in the finite differences scheme of the model in the most accurate way.

The continuity equation $\nabla \cdot \mathbf{u} = 0$ integrated over the volume between two outcropping isopycnals in the mixed layer yields:

$$\iiint_V \nabla \cdot \mathbf{u} \, dv = \iint_s \mathbf{u} \cdot \mathbf{n} \, ds = 0$$

where S is the surface bounding the volume V of water between densities ρ_1 and ρ_2 and the mixed layer base. Separating the surface integral into lateral (S_l) and bottom (S_b) contributions (see Fig. 10), where "lateral" means the largely vertical density surfaces at ρ_1 and ρ_2, and "bottom" means the base of the mixed layer, we obtain:

$$\iint_{s_l} \mathbf{u} \cdot \mathbf{n} \, ds_l + \iint_{s_b} \mathbf{u} \cdot \mathbf{n} \, ds_b = 0. \tag{7}$$

Here $\mathbf{n}$ is the local outward pointing unit normal to the surface (either s_l or s_b). The first

integral above can be computed directly from model horizontal velocities. This calculation is straightforward and accurate. The second can be rewritten as:

$$\iint_{s_b} (w\mathbf{k} \cdot \mathbf{n} + \mathbf{u}_H \cdot \mathbf{n})\, ds_b. \tag{8}$$

Rewriting the normal vector to the base of the mixed layer $\mathbf{n}$ as $-(\mathbf{k} + \nabla_H h)/(1 + |\nabla_H h|^2)^{1/2}$, Eq. 7 becomes:

$$\iint_{s_l} \mathbf{u} \cdot \mathbf{n}\, ds_l + \iint_{s_b} \frac{-w - \mathbf{u}_H \cdot \nabla h}{(1 + |\nabla_H h|^2)^{1/2}}\, ds_b = 0.$$

The use of Eq. 6 and the fact that $ds_b/(1 + |\nabla_H h|^2) = dA$ gives:

$$\iint_{s_l} \mathbf{u} \cdot \mathbf{n}\, ds_l + \iint_{s_b} (d_e + h_t)\, dA = 0$$

and

$$\iint_{s_b} d_e\, dA = -\iint_{s_b} h_t\, dA + \iint_{s_l} \mathbf{u} \cdot \mathbf{n}\, ds_l. \tag{9}$$

Recalling the discrete formulation of our numerical model, the instantaneous subduction rate is obtained by summing over the grid boxes between the two outcropping densities:

$$\begin{aligned} D_e &= \sum_{n=1}^{nboxes} \iint_{s_b} d_e(n)\, dA \\ D_e &= -\sum_{n=1}^{nboxes} h_t(n)\, dA(n) - \sum_{n=1}^{nboxes} \mathbf{u} \cdot \mathbf{n}\, ds_l(n) \end{aligned} \tag{10}$$

Note that in this formulation, derived with the use of the continuity equation, the subduction rate does not explicitly require the vertical velocity, a quantity which is obtained from a diagnostic calculation and is usually noisy in numerical models.

REFERENCES

Barnier, B., P. Marchesiello, A. P. de Miranda and M. Coulibaly. 1998. A sigma-coordinate primitive equation model for studying the circulation in the South Atlantic. Part I: Model configuration with error estimates. Deep-Sea Res., *45,* 543–572.

Barnier, B., L. Siefridt and P. Marchesiello. 1995. Thermal forcing for a global ocean circulation model using a three-year climatology of ECMWF analyses. J. Mar. Syst., *6,* 363–380.

Beckmann, A. and D. Haidvogel. 1993. Numerical simulation of flow around a tall isolated seamount. Part I: Problem formulation and model accuracy. J. Phys. Oceanogr., *23,* 1736–1753.

Cummins, P. F., G. Holloway and A. E. Gargett. 1990. Sensitivity of the GFDL ocean general circulation model to a parameterization of vertical mixing. J. Phys. Oceanogr., *20,* 817–830.

Cushman-Roisin, B. 1987a. On the role of heat flux in the Gulf Stream-Sargasso Sea subtropical gyre system. J. Phys. Oceanogr., *17,* 2189–2022.

—— 1987b. Subduction, *in* Dynamics of the Oceanic Surface Mixed Layer, P. Muller and D. Anderson, eds., Hawaii Inst. of Geophysics Special Publications, 181–196.

Deacon, G. E. R. 1937. The hydrology of the Southern Ocean. Discovery Reports, *15,* 1–124.

de Miranda, A. P. 1996. Application d'un modèle numérique de circulation générale océanique permettant la turbulence de méso-échelle à l'étude de l'Atlantique Sud. PhD thesis, Université Joseph Fourier, Grenoble 1, France.

de Miranda. A. P., B. Barnier and W. K. Dewar. 1999. On the dynamics of the Zapiola Anticyclone. J. Geophys. Res., (in press).

Dewar, W. K. 1986. On the potential vorticity structure of weakly ventilated isopycnals: A theory of subtropical mode water maintenance. J. Phys. Oceanogr., *16,* 1204–1216.

—— 1998. Topography and barotropic transport control by bottom friction. J. Mar. Res., *56,* 295–328.

Gordon, A. L. 1981. South Atlantic thermocline ventilation. Deep-Sea Res., *28*(11), 1239–1264.

Haidvogel, D. B., J. L. Wilkin and R. Young. 1991. A semi-spectral primitive equation ocean circulation model using vertical sigma and orthogonal curvilinear horizontal coordinates. J. Comp. Phys., *94,* 151–185.

Jenkins, W. 1982. On the climate of a subtropical ocean gyre: Decade timescale variations in water mass renewal in the Sargasso Sea. J. Mar. Res., *40*(Suppl.), 265–290.

Joyce, T. and P. Robbins. 1996. The long term hydrographic record at Bermuda. J. Climate, *9,* 3121–3131.

Levitus, S. 1982. Climatological atlas of the world ocean. Geophysical Fluid Dynamics Laboratory, Princeton University, Princeton, NJ.

Luyten, J. R., J. Pedlosky and H. Stommel. 1983. The ventilated thermocline. J. Phys. Oceanogr., *13,* 292–309.

Marchesiello, P., B. Barnier and A. P. de Miranda. 1998. A sigma-coordinate primitive equation model for studying the circulation in the South Atlantic. Part II: Meridional transports and seasonal variability. Deep-Sea Res., *45,* 573–608.

Marshall, J. C., A. J. G. Nurser and R. G. Williams. 1993. Inferring the subduction rate and period over the North Atlantic. J. Phys. Oceanogr., *23,* 1315–1329.

Masuzawa, J. 1969. Subtropical mode water. Deep-Sea Res., *16,* 463–472.

McCartney, M. S. 1977. Subantarctic Mode Water, *in* A Voyage of Discovery, George Deacon 10th Anniversary Volume, Deep Sea Res. (Suppl)., 103–119.

—— 1982. The subtropical recirculation of mode water. J. Mar. Res., *40,* 427–464.

Ollitrault, M. 1998. The AAIW general circulation in the Brazil Basin and Equatorial Atlantic, *in* Proceedings of the WOCE Conference, Ocean Circulation and Climate, Halifax, Canada.

Peterson, R. G. and T. Whitworth. 1989. The subantarctic and polar fronts in relation to deep water masses through the southwestern Atlantic. J. Geophys. Res., *94*(C8), 10817–10838.

Provost, C., S. Gana, V. Garçon, K. Maamaatuaiahutapu and M. England. 1995. Hydrographic conditions in the Brazil-Malvinas Confluence during austral summer 1990. J. Geophys. Res., *100*(C6), 10655–10678.

Qiu, B. and X. Huang, R. 1995. Ventilation of the North Atlantic and North Pacific: Subduction versus obduction. J. Phys. Oceanogr., *25,* 2374–2390.

Rhines, P. B. and W. R. Young. 1982. Homogenization of potential vorticity in planetary gyres. J. Fluid Mech., *122,* 347–367.

Samelson, R. and G. Vallis. 1997. Large-scale circulation with small diapycnal diffusion: The two-thermocline limit. J. Mar. Res., *55,* 223–275.

Saunders, P. M. and B. A. King. 1995a. Bottom currents derived from a shipborne ADCP on the WOCE Cruise A11 in the South Atlantic. J. Phys. Oceanogr., *25,* 329–347.

—— 1995b. Oceanic fluxes on the WOCE A11 Section. J. Phys. Oceanogr., *25,* 1942–1958.

Siefridt, L. 1994. Validation des données ERS-1 et des flux de surface du CEPMMT dans le contexte de la modélisation des circulations océaniques à l'échelle d'un bassin. PhD thesis, Université Joseph Fourier, Grenoble 1, France.

Song, Y. and D. Haidvogel. 1993. Numerical simulations of the CCs under the joint effects of coastal geometry and surface forcing, *in* Estuarine and Coastal Modeling III, Proceedings of the 3rd Int'l Conference, 216–234.

Speer, K. G. and E. Tziperman. 1992. Rates of water mass formation in the North Atlantic Ocean. J. Phys. Oceanogr., *22,* 93–104.

Stommel, H. 1979. Determination of watermass properties of water pumped down from the Ekman layer to the geostropic flow below. Proc. Natl. Acad. Sci. U.S., *76,* 3051–3055.

Talley, L. D. and M. E. Raymer. 1982. Eighteen degree water variability. J. Mar. Res., *40*(Suppl.), 757–775.

Tréguier, A. M. 1992. Kinetic energy analysis of an eddy resolving, primitive equation model of the North Atlantic. J. Geophys. Res., *97,* 687–701.

Tsuchiya, M. M., L. D. Talley and M. S. McCartney. 1994. Water-mass distribution in the western South Atlantic; A section from South Georgia Island (54S) northward across the equator. J. Mar. Res., *52,* 55–81.

Walin, G. 1982. On the relation between sea-surface heat flow and thermal circulation in the ocean. Tellus, *34,* 187–195.

Warren, B. 1972. Insensitivity of subtropical mode water characteristics to meteorological fluctuations. Deep-Sea Res., *19,* 1–19.

Weatherly, G. L. 1993. On deep-current and hydrographic observations from a mudwave region and elsewhere in the Argentine Basin. Deep-Sea Res., *40*(Part II), 851–858.

Whitworth, T. and W. D. Nowlin. 1987. Water masses and currents of the Southern Ocean at the Greenwich Meridian. J. Geophys. Res., *92,* 6462–6476.

Worthington, L. V. 1959. The 18° water in the Sargasso Sea. Deep-Sea Res., *5,* 297–305.

Received: *25 June, 1998;* revised: *22 December, 1998.*